

Superconductivity in the Face Centered Cubic $W_{n-x}Mo_xRhIrPt_2$ High Entropy Alloy

Denver Strong and R. J. Cava

Department of Chemistry Princeton University, Princeton NJ

Abstract

We report single phase superconducting face centered cubic (FCC) high entropy alloys (HEAs) synthesized via splat cooling. The single phase materials fall at electron counts in the HEA superconductor alloy family where structural stability and optimal superconducting electron counts clash. The materials' superconducting properties follow the general trends published for metallic alloys. Many of the superconducting characteristics are summarized. Insights are provided as to why an FCC structure may be stable.

Introduction

High entropy alloys (HEAs) are one of the newest material classes, being studied for fewer than fifteen years.^[1,2] They are typically defined as consisting of five or more elements, each of less than 35% concentration, ensuring that no single element dominates the observed properties.^[3] Even assuming that element selection is restricted to the 30 transition metals, and that a five-component HEA must be equimolar, then there are on the order of 10^6 options for such alloys. If including elements beyond the transition metals, and varying their contents from equimolar, the possibilities are nearly endless - a particularly useful characteristic when tuning an alloy to obtain a specific property.

Although in practice the thermodynamics are more nuanced, the basic idea is straightforward. Using equation 1,

$$\Delta G_{mix} = \Delta H_{mix} - T\Delta S_{mix} , \quad (1)$$

the goal for formation of HEA's is to make the term in the above expression that represents the product of temperature times the entropy of mixing (ΔS_{mix}) very large. Including more elements increases the entropy of mixing. Paired with a high temperature T but not limited to those achievable by arc melting, the second term overcomes any of the enthalpic effects of the first (ΔH_{mix}), and a solid solution can sometimes form.^[2,3] When more elements are available, and faster cooling rates from high temperature are employed, (which maximizes the impact of ΔS_{mix}); sometimes there is no segregation into a mixture of phases whose stability is dominated by a negative ΔH_{mix} and a high entropy solid solution can form on a simple lattice. These solid

solutions are typically body-centered cubic (BCC), hexagonal close packed (HCP), or face-centered cubic (FCC), but more recent papers are showing that entropically stabilized solid solutions can form topologically close packed structures as well and are not necessarily straightforward.^[4-8]

HEAs can display a wide variety of physical properties, including magnetism, good corrosion resistance, excellent mechanical properties, and superconductivity.^[3,9] However, a superconducting face-centered cubic solid solution has not been reported to-date.^[10] A superconducting FCC HEA is desired for applications due to a high ductility associated with the increased number of slip systems in the structure.^[11] FCC superconductors haven't completely eluded researchers, however, because they exist for binary alloys; but they have been difficult to observe within the high entropy regime. Why this has been difficult is revealed in Figure 1. The face centered cubic structure is stable, following a hard sphere model, when more than 8 valence electrons per atom (i.e. the VEC) are available.^[12] Below that, a change of the stacking from FCC type to HCP type is expected to occur. This has been explained as resulting from increased hybridization.^[12] The stable FCC VEC is not one that is favored for superconductivity, however, and thus the co-existence of HEA superconductivity and the FCC structure has not been observed. This issue is illustrated in Figure 1, which shows the difficulties in finding a high entropy superconducting FCC solid solution - the structure is only stable for VECs that are outside of the superconducting VEC regime. There are not yet a sufficient number of anomalies known to consistently shift the maximum VEC threshold for superconductivity up in electron count or the VEC threshold for FCC stability down in electron count for both superconductivity and an FCC crystal structure to co-exist in the same material.

Here, we report high entropy materials derived from the anomalous binary FCC solid solution, $W_{67}Pt_{33}$, which superconducts at 3.0 K.^[13] The Mo-W-Rh-Ir-Pt alloys studied here contain no principle elements, and none of the elements by itself superconducts above 1 K, yet the reported alloys have a maximum $T_c=1.5$ K. The VEC bounds on structure suggest that an HCP alloy should form rather than FCC, and structure-in-structure-out (SISO) methods predict that a BCC structure should form before entering the high entropy regime.^[3] Nonetheless we present proof that something different happens under our synthetic conditions.

This paper is summarized as follows. The next sections describe the synthesis, structural and physical characterization methods. The structural results are described in section 3 while

section 4 addresses the superconducting properties. Finally, section 5 summarizes the physical properties, and addresses where these results lead.

Methods

The samples were made from elemental powders, total weight less than 200 mg, ground in stoichiometric ratios and compressed in a steel die to form a pellet. The pellets were arc melted 5x on a water-cooled copper hearth with $I \sim 50$ A, $V \sim 480$ V, in an argon atmosphere after a zirconium getter was used to remove residual oxygen. This procedure ensures that the elements were well mixed. Samples were then placed in a copper well with a zirconium getter again. The hearth was then heated with $I \sim 50$ A for 5-8 s before immediately aiming the arc toward the sample in the bottom of the copper well. Heating continued for another 5-8 s after the molten state had been reached. The tungsten electrode was then removed from the well and a spring-loaded copper cooling tip immediately plunged into the molten liquid, quenching it into the solid state. The result was a thin solidified sheet ($t < 0.6$ mm) sample that could be broken into flakes. The “best” (i.e. single phase) samples were the thinnest after the splat quench.

Diffraction patterns were collected in the Bragg Brentano geometry on a Bruker D8 Advance ECO diffractometer, using Cu $K\alpha$ X Rays. Resistivity and heat capacity measurements were performed on the largest and smallest remaining flakes, respectively, in a Quantum Design Physical Property Measurement System (PPMS), via a standard 4 probe resistivity puck on an adiabatic refrigeration (ADR) attachment, and a ^3He heat capacity puck.

Results

Figure 2 shows the pXRD patterns for select samples of $\text{W}_{2-x}\text{Mo}_x\text{RhIrPt}_2$ ($\text{W}_{33-x}\text{Mo}_x\text{Rh}_{17}\text{Ir}_{17}\text{Pt}_{33}$), with x values selected to result in alloy compositions of 0, 5, and 10% Mo. All the samples display clear $K\alpha_1/K\alpha_2$ splitting for the diffraction lines, indicative of highly crystalline uniform alloys. In the 10% Mo sample, for example, the nominal concentration is $\text{W}_{23}\text{Mo}_{10}\text{Rh}_{17}\text{Ir}_{17}\text{Pt}_{33}$, which is clearly within the HEA regime. Each pattern was refined using GSAS-II, with lattice parameters as summarized in Table 2. The samples are very clearly FCC. There are occasionally minor HCP peaks present and noted, but they represent such a small concentration of precipitate that they do not interfere with our interpretation of the data.

It is common practice to consider intermetallic alloys in terms of the Hume-Rothery rules, where weighted variations are used to identify the robustness of the system. The standard equations employed to calculate the allowed variations in atomic radii and electronegativity are, respectively,^[14]

$$\delta = 100 \sqrt{\sum_{i=1}^n c_i \left(1 - \frac{r_i}{\underline{r}}\right)^2}, \quad (2)$$

$$\Delta\chi = \sqrt{\sum_{i=1}^n c_i (\chi_i - \underline{\chi})^2}. \quad (3)$$

The underlined values are weighted averages while c_i , r_i , and χ_i are the concentration, atomic radii, and Pauling electronegativity of each element. δ and $\Delta\chi$ values less than 10% are generally taken as systems that satisfy the Hume-Rothery rules. The values for our system are summarized in Table 2.

Finally, the expected enthalpy of mixing can be approximated by

$$\Delta H_{mix} = \sum_{i=1, j \neq i}^n 4\Delta H_{ij} c_i c_j, \quad (4)$$

where ΔH_{ij} is the mixing enthalpy of binary liquid alloys.^[14] In the current analysis, the values for ΔH_{ij} are taken from the literature^[15] and are included in the supplementary material. When the FCC superconductors reported here are compared with other high entropy superconducting solid solutions, in Figure 3, they are seen to display the smallest δ values. However, the negative mixing enthalpies suggest the alloys are members of a non-ideal, regular solution. This may be one of the best examples known where a largely negative mixing enthalpy can aid in the formation of a solid solution.^[3]

Recently, the mysteries of metallic bonding in transition metals has piqued some interest.^[16] We briefly summarize, and then conceptualize, a proposal in the literature for why these alloys form from a microscopic viewpoint. In close packed systems, each Wyckoff cell has two types of energetic cages — tetrahedral (point P in Figure 4) and octahedral (point H in Figure 4). In between them is a ‘ring critical point’ on the Wyckoff surface. This means that the point’s electron density changes only along one direction which is along the Wyckoff edge. For the early transition metals, the location of this particular critical point begins near the tetrahedral cage, an electron deficient vertex where three edges come together. As we traverse across the d element series, the critical point moves toward the octahedral cage – the vertex where four edges

come together. With these two well- defined energetic basins, the stability as a function of electron count can be explained by looking at which vertex collects kinetic energy faster with the addition of more electrons.^[16] Elements to the left of Rh collect kinetic energy in the tetrahedral cage faster while the FCC elements to right, including Rh itself, collect energy faster in the octahedral cage. Considering the high temperature synthesis required for formation, the reported alloys must be in a position such that the tetrahedral cage collects kinetic energy faster than the octahedral cage at low temperatures, but the opposite is true at high temperatures. Ultimately, the sample must be sufficiently mixed so the octahedral electron density of FCC formers can flood the tetrahedral cage of HCP formers at high temperatures. Once *all* the shallow cages are filled, the residual energy collects in the octahedral basin. The importance of this kinetic energy has been discussed previously when considering the formation of a pseudogap in metallic alloys.^[17]

Superconductivity

Typically, magnetization data would be taken to confirm the presence of a Meissner effect for a superconductor, but unfortunately all of the T_c values for the materials prepared here are below the low temperature limit of our magnetometer (1.8 K). Most of the following analysis is therefore limited to adiabatic refrigeration and ^3He measurements, which allows for the determination of the temperature-dependent resistivity to low temperatures. However, we can measure a superconducting transition of a Mo-free medium entropy alloy (MEA) near 1.85 K, $\text{W}_4\text{RhIrPt}_2$ ($\text{W}_{50}\text{Rh}_{13}\text{Ir}_{13}\text{Pt}_{25}$). This transition can be characterized in a magnetic field above 1.8 K, giving an estimate of the upper critical field of these alloys. (There is a minute fraction of impurity with $T^{\text{onset}} \sim 2.5$ K present, although it is not observed in the powder pattern for this sample - where the sensitivity is estimated to be at the level of 1%.) Although the XRD analysis indicates that this sample is a pure phase, low temperature heat capacity measurements show the transition may not be intrinsic. The resistive transition is 85% above the heat capacity jump, and the size of the jump is small in comparison to other superconductors. There must be an immeasurable amount of W-rich impurity present that lowers the VEC and hence increases the critical temperature measured resistively. This is important to note, because our overall trends follow the results from the binary material, which may be worth interpreting with caution moving forward. These results are included in the supplemental information so as to not mislead the reader.

Low temperature resistivity data is shown in figure 5 along with points for every alloy reported here alongside reproduced values from the original binary.^[13] It was previously explained that linear trends in T_c suggest that the electronic density of states' landscape is relatively unchanged as the electron count is varied.^[13] This is the situation seen in W-Pt superconductors but the most disordered system gives a significant drop in critical temperature. Here, we're changing the electronic structure, but maintaining the VEC. Since Mo is the least electronegative of the five, we've likely shifted the linear region of the DOS above the fermi energy, hence yielding a drastic decrease in T_c . This is due to the electronegativity difference of the elements, not disorder, though. An alternative explanation is that enough Mo has been included to bypass the solid solution frontier of the multi-dimensional phase diagram. If the microstructure has changed, the bonding pseudogap may be larger and hence the DOS is not as sharp as suggested in Figure 5.

Sufficiently thin samples have $\Delta T_c \sim 0.2$ K from the onset of the resistivity transition to 0 resistivity, which suggests that the increased disorder present does not generally increase the electronic inhomogeneity within the samples when they are appropriately splat cooled. This appears to be contrary to other reports where broadening of the superconducting transition is seen for HEAs^[18-27] prepared by conventional arc melting - the slower cooling rates for arc-melted samples give time for atoms to give different local structures. Provided that there's not a more metastable state present for splat-cooled vs. as-cast alloys, the splat cooling synthesis method may be expected to pin down more exact critical temperatures for random homogenous mixtures.

The superconductivity in our other alloys is clearly delineated through our ^3He heat capacity measurements where a lower temperature is experimentally available. The transitions for the HEAs are incomplete above the minimum temperature of the ^3He apparatus making it difficult to fully characterize.

Considering the results for $\text{W}_4\text{RhIrPt}_2$ ($\text{W}_{50}\text{Rh}_{12.5}\text{Ir}_{12.5}\text{Pt}_{25}$), we study the system with the next highest T_c , $\text{W}_{3.5}\text{RhIrPt}_2$ ($\text{W}_{46.7}\text{Rh}_{13.3}\text{Ir}_{13.3}\text{Pt}_{26.7}$). A broad transition occurs at $T \sim 1.5$ K. With the addition of the Schottky anomaly, it's difficult to pinpoint a transition temperature to determine the superconducting jump. However, it's clear from figure 6 the transition is between $1.3 \text{ K} < T < 2.0 \text{ K}$. The high temperature side was fit to

$$\frac{c}{T} = (5.75 \cdot 10^{-5})T^4 + (6.47 \cdot 10^{-2})T^2 + 2.92, \quad (5)$$

Where x is the independent variable, T^2 . From this, we determine the Sommerfeld constant to be $2.92 \text{ (mJ/mol.K}^2\text{)}$, and we can approximate the Debye temperature as^[6]

$$\theta_D = \sqrt[3]{\frac{12\pi^4 N_A k_B}{5 \cdot 6.47 \cdot 10^{-2}}} = 311 \text{ K}, \quad (6)$$

each of which are lower than the weighted averages of the individual elements ($\gamma = 3.25 \text{ mJ/mol.K}^2$, $\theta = 366 \text{ K}$).

The common equal areas approach suggests a $T_c \sim 1.5 \text{ K}$, and hence a $\frac{\Delta C}{\gamma T_c} \sim 1.23$. This value is only slightly smaller in comparison to what should be seen theoretically for BCS superconductors (1.43), indicating a bulk, BCS superconductor. The electron-phonon interaction can then be quantified using McMillan's equation^[30]

$$\lambda_{e-ph} = \frac{1.04 + \mu^* \ln(\theta_D / 1.45 T_c)}{(1 - 0.62 \mu^*) \ln(\theta_D / 1.45 T_c) - 1.04}. \quad (8)$$

Assuming $\mu^* = 0.13$, equation (8) returns $\lambda_{e-p} \sim 0.42$, which is only slightly below the average and median values of other alloys.^[30]

Discussion and Conclusion

Although it's similar, superconductivity is cut short in these alloys when compared to the W-Pt binary. It was previously pointed out the alloying in this binary system is not straightforward, because there's an initial decrease in the lattice parameters when W is added to Pt before the curve turns over to follow Vegard's law.^[13] Cooper pairs don't form until after this minimum is reached, and the still uncharacterized electronic structure of the low doped Pt disappears. However, it's the help of this alloy, along with the fast cooling rates accessible by splat cooling, that allow high quality FCC superconducting HEAs to form.

An HCP phase, the expected form, could not be isolated at the HEA composition to allow for a direct comparison of the T_c s in the different structure types with all other factors being the same. This is likely due to neighboring FCC formers retaining their octahedral kinetic energy; it would be easier to compare two polymorphs in a simpler system. Whether or not the FCC crystal structure for these alloys is truly a metastable state or it's thermodynamically stable when held below the liquidus temperature is not known.

In terms of superconductivity, when compared to previously published trends, these materials do stand out strictly due to their small superconducting heat capacity jump – an

important observation because of the discrepancy from BCS theory. They continue to follow previously reported T_c vs VEC trends, although they do have very narrow resistive transitions when compared to typical HEA superconductors,^[18-27] this is likely due to the synthesis method employed. Superconducting FCC HEAs are interesting systems to study moving forward due to their location between structural and superconducting stability boundaries, work which may help to illuminate the limits of BCS theory.

Acknowledgement

This research was funded by the Gordon and Betty Moore Foundation, grant number GBMF-9066

References

- 1) Cantor, Brian, et al. "Microstructural development in equiatomic multicomponent alloys." *Materials Science and Engineering: A* 375 (2004): 213-218.
- 2) Yeh, J-W., et al. "Nanostructured high-entropy alloys with multiple principal elements: novel alloy design concepts and outcomes." *Advanced Engineering Materials* 6.5 (2004): 299-303.
- 3) Miracle, Daniel B., and Oleg N. Senkov. "A critical review of high entropy alloys and related concepts." *Acta Materialia* 122 (2017): 448-511.
- 4) Liu, Bin, et al. "Formation and superconductivity of single-phase high-entropy alloys with a tetragonal structure." *ACS Applied Electronic Materials* 2.4 (2020): 1130-1137.
- 5) Liu, Bin, et al. "Superconductivity and paramagnetism in Cr-containing tetragonal high-entropy alloys." *Journal of Alloys and Compounds* 869 (2021): 159293.
- 6) Stolze, Karoline, et al. "High-entropy alloy superconductors on an α -Mn lattice." *Journal of Materials Chemistry C* 6.39 (2018): 10441-10449.
- 7) Liu B, Wu JF, Cui YW, Zhu QQ, Xiao GR, Wang HD, et al. Structural evolution and superconductivity tuned by valence electron concentration in the Nb–Mo–Re–Ru–Rh high-entropy alloys. *J Mater Sci Technol* (2021) 85:11. doi:10.1016/j.jmst.2021.02.002
- 8) Browne, A.J.; Strong, D.P.; Cava, R.J. Stability and superconductivity of 4d and 5d transitional metal high-entropy alloys. arXiv 2021, arXiv:2109.10043. Available online: <https://arxiv.org/abs/2109.10043> (accessed 23 Dec 2022)
- 9) Lee, Yea-Shine, and Robert J. Cava. "Superconductivity in high and medium entropy alloys based on MoReRu." *Physica C: Superconductivity and its Applications* 566 (2019): 1353520.
- 10) Ishizu, N.; Kitagawa, J. Trial of a search for a face-centered-cubic high-entropy alloy superconductor. arXiv 2020, arXiv:2007.00788. Available online: <https://arxiv.org/abs/2007.00788> (accessed on 23 Dec 2022).
- 11) Callister Jr., W.D.; *Materials Science and Engineering an Introduction*. In *Dislocations and Strengthening Mechanisms*; John Wiley & Sons Inc. 2000; pp 153-184.
- 12) Pettifor, D. G. "Theory of the crystal structures of transition metals." *Journal of Physics C: Solid State Physics* 3.2 (1970): 367.
- 13) LUO H-L 19683. *Less Common Metals* 15 299-302
- 14) Sheng, G. U. O., and Chain Tsuan Liu. "Phase stability in high entropy alloys: Formation of solid-solution phase or amorphous phase." *Progress in Natural Science: Materials International* 21.6 (2011): 433-446.
- 15) Boer, F.R. de, Mattens, W C.M., Boom, R, Miedema, A R, and Niessen, A K. Cohesion in metals. Transition metal alloys. Netherlands: N. p., 1988. Web.
- 16) S. K. Riddle, T. R. Wilson, M. Rajivmoorthy and M. E. Eberhart, *Molecules*, 2021, 26, 5396.
- 17) Mizutani, U.; Sato, H. The physics of the Hume-Rothery electron concentration rule. *Crystals* 2017, 7, 9.
- 18) P. Koželj, S. Vrtnik, A. Jelen, S. Jazbec, Z. Jagličić, S. Maiti, M. Feuerbacher, W. Steurer, and J. Dolinšek, *Phys. Rev. Lett.* 113, 107001 (2014).

- 19) F. von Rohr, M. J. Winiarski, J. Tao, T. Klimczuk, and R. J. Cava, Proc. Nat. Acad. Sci. USA 113, E7144 (2016).
- 20) F. O. von Rohr and R. J. Cava, Phys. Rev. Mater. 2, 034801 (2018).
- 21) Kim, G.; Lee, M.-H.; Yun, J.H.; Rawat, P.; Jung, S.-G.; Choi, W.; You, T.-S.; Kim, S.J.; Rhyee, J.-S. Strongly correlated and strongly coupled s-wave superconductivity of the high entropy alloy Ta₁/6Nb₂/6Hf₁/6Zr₁/6Ti₁/6 compound. *Acta Mater.* **2020**, *186*, 250–256.
- 22) Wu, K.-Y.; Chen, S.-K.; Wu, J.-M. Superconducting in equal molar NbTaTiZr-based high-entropy alloys. *Nat. Sci.* **2018**, *10*, 110–124.
- 23) Marik, S.; Varghese, M.; Sajilesh, K.P.; Singh, D.; Singh, R.P. Superconductivity in equimolar Nb-Re-Hf-Zr-Ti high entropy alloy. *J. Alloys Compd.* **2018**, *769*, 1059–1063.
- 24) Ishizu, N.; Kitagawa, J. New high-entropy alloy superconductor Hf₂₁Nb₂₅Ti₁₅V₁₅Zr₂₄. *Res. Phys.* **2019**, *13*, 102275.
- 25) Lee, Y.-S.; Cava, R.J. Superconductivity in high and medium entropy alloys based on MoReRu. *Phys. C* **2019**, *566*, 1353520.
- 26) Marik, S.; Motta, K.; Varghese, M.; Sajilesh, K.P.; Singh, D.; Breard, Y.; Boullay, P.; Singh, R.P. Superconductivity in a new hexagonal high-entropy alloy. *Phys. Rev. Mater.* **2019**, *3*, 060602(R).
- 27) Liu, B.; Wu, J.; Cui, Y.; Zhu, Q.; Xiao, G.; Wu, S.; Cao, G.; Ren, Z. Superconductivity in hexagonal Nb-Mo-Ru-Rh-Pd high-entropy alloys. *Scr. Mater.* **2020**, *182*, 109–113.
- 28) Matthias, Bernd T. "Empirical relation between superconductivity and the number of valence electrons per atom." *Physical review* 97.1 (1955): 74.
- 29) Toby, B. H., & Von Dreele, R. B. (2013). "GSAS-II: the genesis of a modern open-source all purpose crystallography software package". *Journal of Applied Crystallography*, **46**(2), 544-549.
- 30) W. L. McMillan, Phys. Rev. 167, 331 1968.

List of Tables

Table 1: Breakdown of elemental properties. ^aRadii, Pauling electronegativity, T_c , γ , and $\theta_D(0\text{ K})$ data were taken from <https://www.knowledgedoor.com/>. ^bThe e/a value is related to the calculated number of itinerant electrons obtained via DFT calculations.^[17]

	Radius [pm] ^a	Pauling Electronegativity ^a	VEC	e/a ^b	T_c [K] ^a	γ [mJ/(mol.K ²)] ^a	$\theta_D(0\text{ K})$ [K] ^a
Mo	141	2.16	6	1.39	0.92	1.83	423
W	141	2.36	6	1.43	0.015	1.01	383
Rh	134	2.28	9	1.00	0.0325	4.65	512
Ir	136	2.20	9	1.60	0.014	3.14	420
Pt	139	2.28	10	1.63	< 0.03	6.54	237

Table 2: A list of all of the newly reported alloys. Shaded yellow alloys are within the high entropy regime. $W_{2.3}Mo_{0.7}RhIrPt_2$ was not characterized because it had a substantial hcp phase. Calculations included here are described in the main text, typically simply weighted standard deviations. Thickness, measured with an electronic dial caliper, is included because thicker samples cooled slower, hence changing the microstructure making the synthesis very technique sensitive.

Logical Formula	True Formula	a[Å]	δ	EN	$\Delta\chi$	Hmix [kJ/mol]	Smix [J/mol.K]	VEC	VEC spread	e/ab	Tc [K]	thickness [mm]
W3.5RhIrPt2	W46.7Rh13.3Ir13.3Pt26.7	3.91627	0.99	2.31	0.02	-16.40	10.36	7.87	0.23	1.45	1.56	0.37
W3RhIrPt2	W42.9Rh14.3Ir14.3Pt28.6	3.90776	1.02	2.30	0.02	-16.17	10.62	8.00	0.22	1.45	1.10	0.19
W2.65Mo0.35RhIrPt2	W37.9Mo5Rh14.3Ir14.3Pt28.6	3.90535	1.03	2.29	0.03	-16.94	11.90	8.00	0.22	1.45	1.25	0.57
W2.3Mo0.7RhIrPt2	W32.9Mo10Rh14.3Ir14.3Pt28.6	3.90382	1.03	2.28	0.03	-17.72	12.55	8.00	0.22	1.45	*	0.28
W2.5RhIrPt2	W38.5Rh15.4Ir15.4Pt30.8	3.90000	1.06	2.30	0.02	-15.68	10.86	8.15	0.21	1.45	0.90	0.48
W2.175Mo0.325RhIrPt2	W33.5Mo5Rh15.4Ir15.4Pt30.8	3.89771	1.07	2.29	0.03	-16.51	12.09	8.15	0.21	1.45	0.85	0.57
W1.85Mo0.65RhIrPt2	W28.5Mo10Rh15.4Ir15.4Pt30.8	3.89765	1.07	2.28	0.03	-17.34	12.69	8.15	0.21	1.45	0.85	0.33
W2RhIrPt2	W33.3Rh16.7Ir16.7Pt33.3	3.89542	1.11	2.29	0.02	-14.77	11.06	8.33	0.20	1.45	0.45	0.26
W1.7Mo0.3RhIrPt2	W28.3Mo5Rh16.7Ir16.7Pt33.3	3.89390	1.11	2.28	0.03	-15.67	12.23	8.33	0.20	1.45	0.40	0.23
W1.4Mo0.6RhIrPt2	W23.3Mo10Rh16.7Ir16.7Pt33.3	3.89085	1.11	2.27	0.03	-16.57	12.75	8.33	0.20	1.45	0.30	0.26

List of Figures

Figure 1:

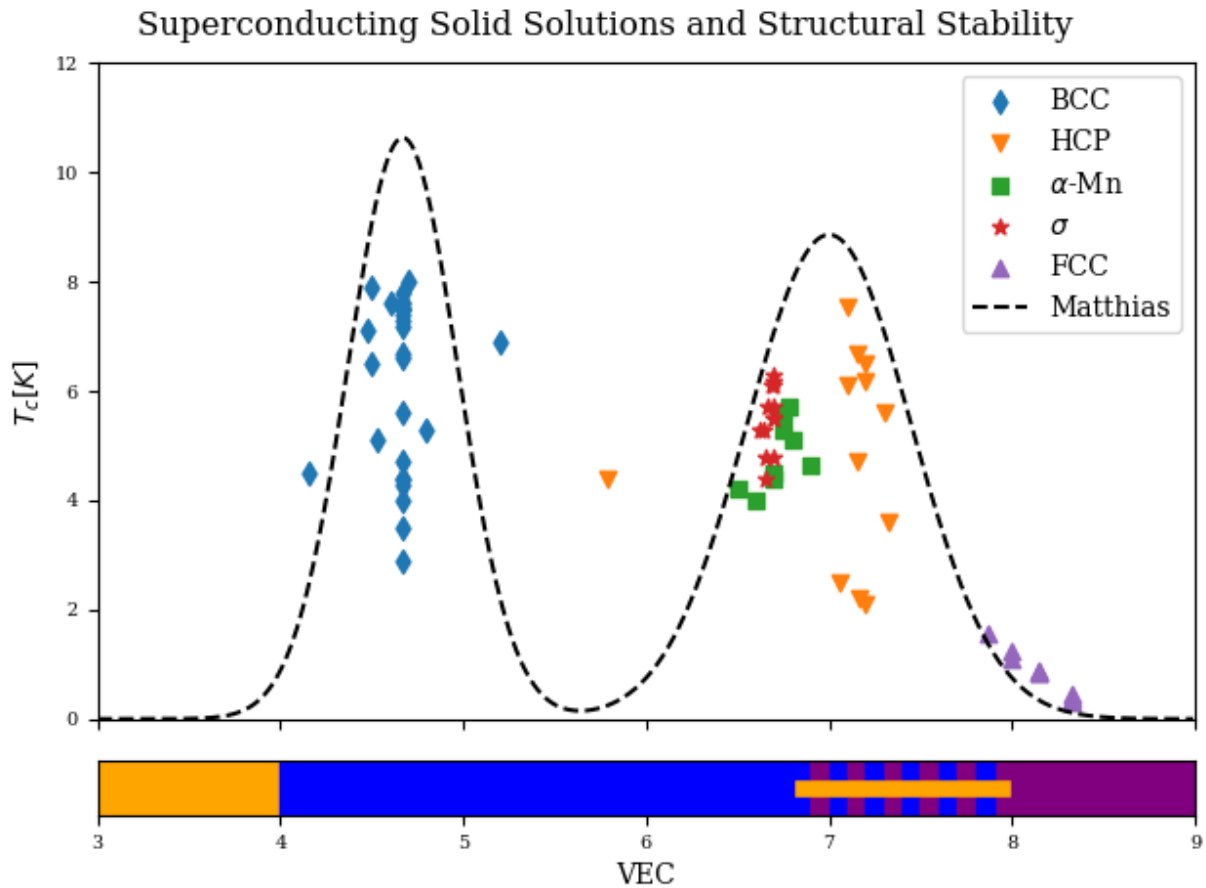


Figure 1: Overlaid plots of T_c and structure stability vs VEC. *Transition Temperature:* The scatter points are a collection of previously reported critical temperatures for high entropy alloys (HEA).^[18-27] The dashed line shows the empirical ‘double hump’ trend for crystalline metal alloys versus valence electron count (VEC).^[28] Calculations for single elements show that the BCC crystal structure is the most stable between VECs of 4 to 6.9 (blue rectangle).^[12] The purple rectangle displays the VEC range where FCC structures are stable, while the yellow is HCP. The region below is an accumulation of experimental stability data. The overlay of the two plots suggests there are not enough anomalies to make a face centered superconductor.

Figure 2:

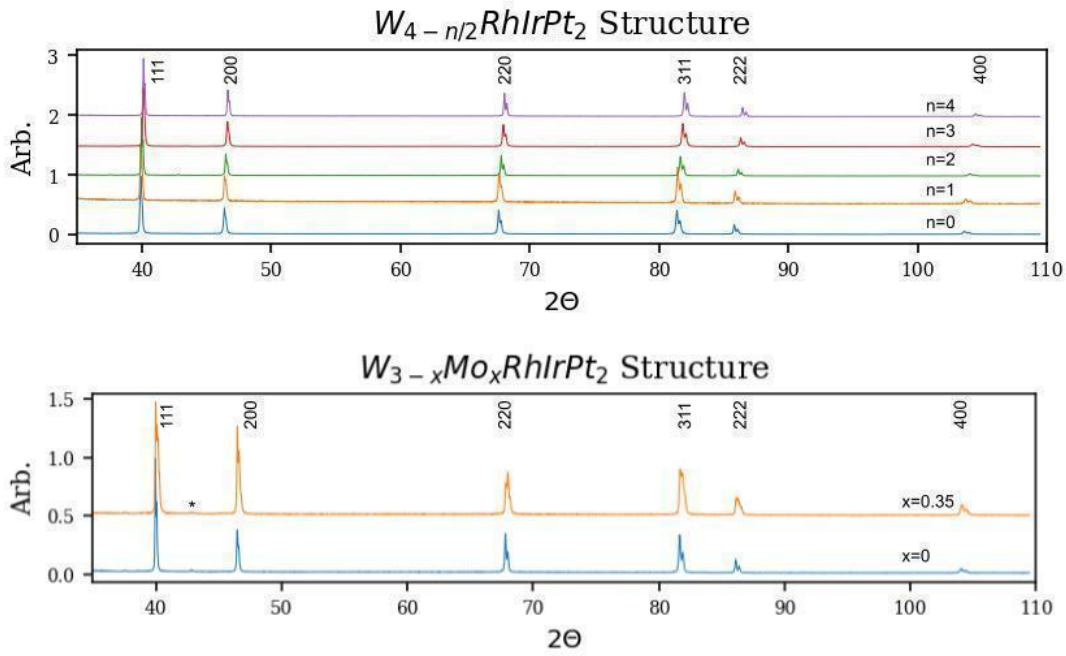


Figure 2: Diffractograms (Cu $K\alpha$ radiation) at ambient temperature for splat cooled $W_{4-n/2}RhIrPt_2$ and $W_{3-x}Mo_xRhIrPt_2$. The results show clear α_1/α_2 splitting in an FCC lattice. A Le bail refinement done with GSAS-II finds the lattice parameters summarized in Table 1.^[29] The * indicates a minor hcp impurity which can be seen more clearly in the raw data. $W_{2.5-x}Mo_xRhIrPt_2$ and $W_{2-x}Mo_xRhIrPt_2$ are included in the supplemental information.

Figure 3:

Solid Solution Phases Between Avg Atomic Radii and Mixing Enthalpy

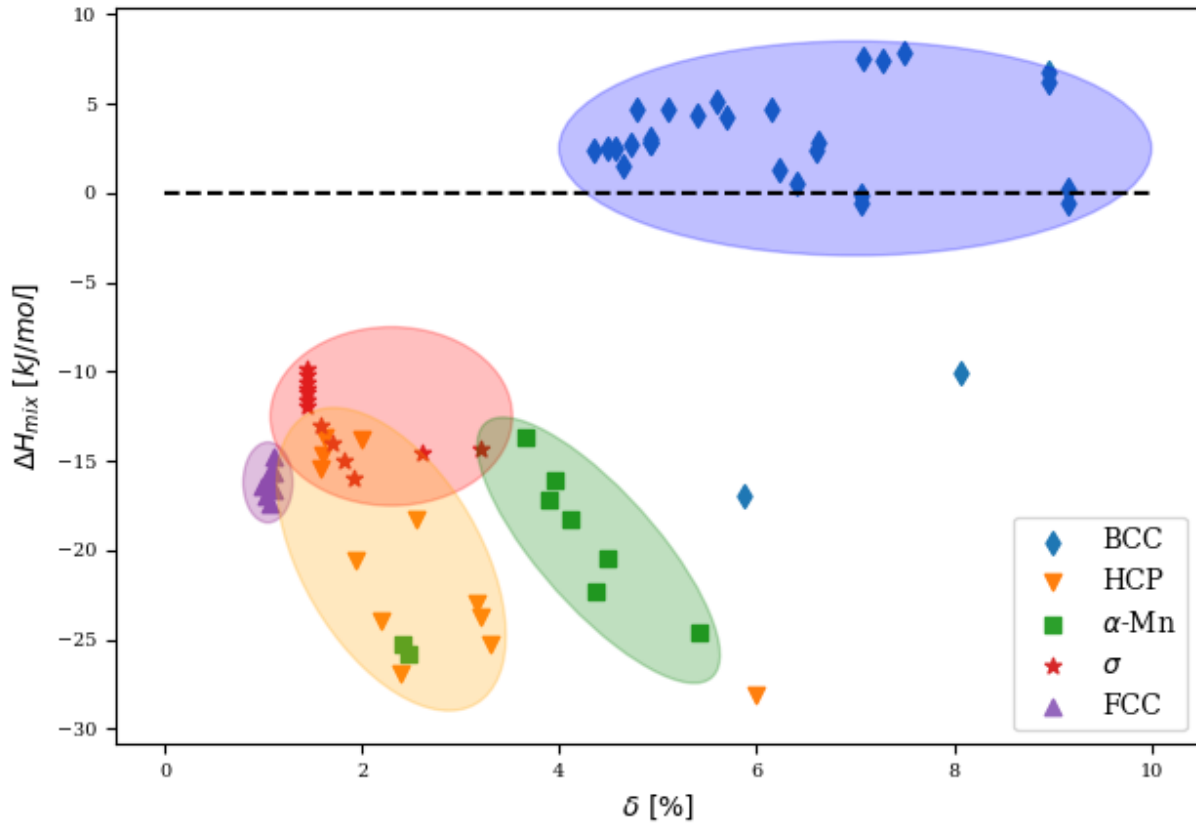


Figure 3: List of high entropy superconducting solid solutions. Plot inspired by reference [3] but limited to solid solution superconductors from refs 18-27 and this work. The FCC alloys are reported in this paper. Solid solutions typically form with small deviations in the atomic radii and small mixing enthalpies. The original Hume-Rothery rules set a boundary below 15% deviation in atomic radii,^[3] but here suggest to stay below 10%. The updated boundaries are wider than the original plot.^[3] It's interesting to note that BCC superconducting alloys seem to be separate from the rest from other superconducting materials (where more negative mixing enthalpies are found regardless of atomic size).

Figure 4:

A Reciprocal Space View of 4d Elements in FCC Structure

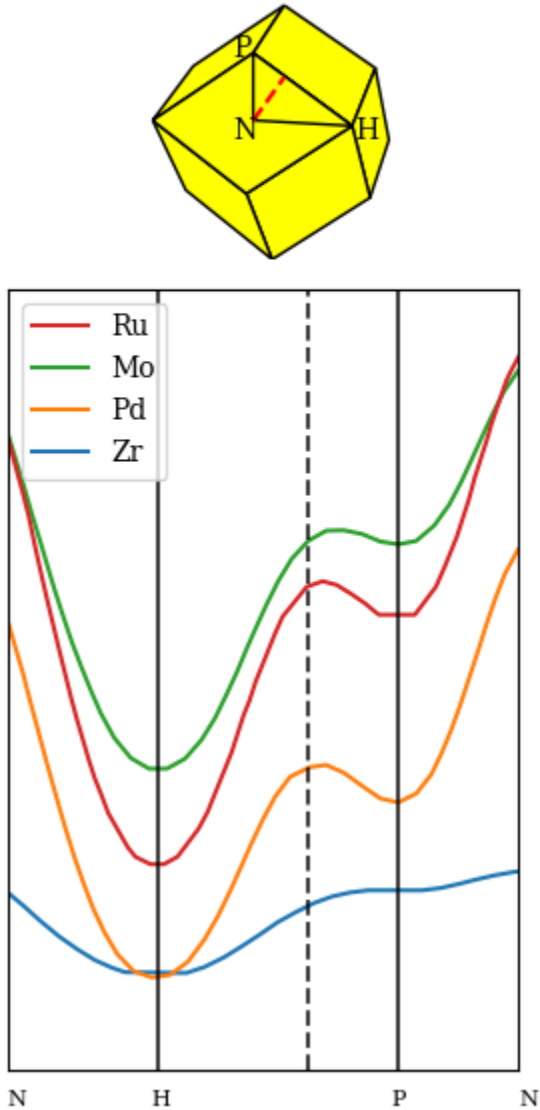


Figure 4: DFT results of 4d transition metals constrained in an FCC structure, reproduced from ref 16. The electron density at the high symmetry points for select 4d transition metals. The tetrahedral cage falls on P, the octahedral cage falls on H, and the ring critical point in an ideal fcc metal falls $\frac{1}{3}$ the edge length from P. When it's too far from $\frac{1}{3}a$, the hcp structure will be preferred.

Figure 5:

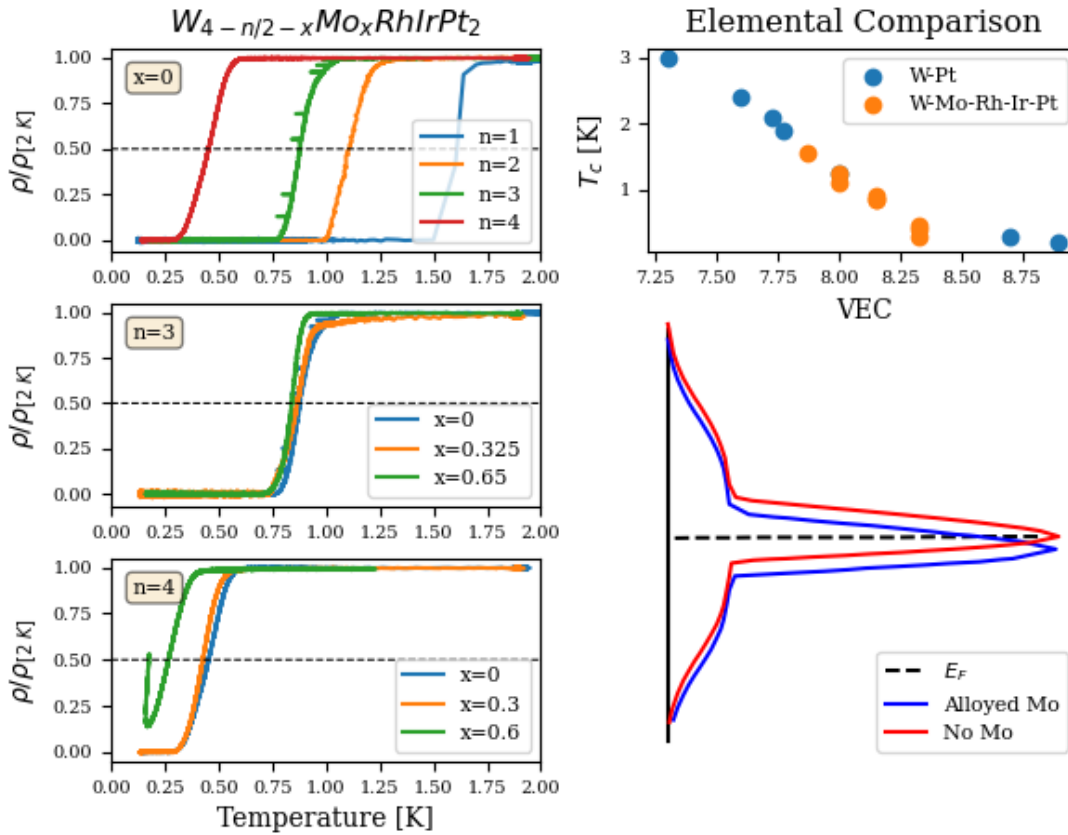


Figure 5: Left) Normalized resistivity plots for pure phase $W_{4-n/2-x}Mo_xRhIrPt_2$ superconductors. Less W clearly pulls down the transition temperature, whereas alloying with Mo seems to have a stronger effect in more disordered systems. The tail for $W_{1.4}Mo_{0.6}RhIrPt_2$ is an artifact of the experiment elaborated on in the supplemental information. **Right)** All newly reported HEA T_c s in comparison with the original W-Pt superconductors versus VEC. The new alloys don't seem to be substantially different at low VECs. There's no clear reason for the abrupt decrease in T_c for $W_{1.4}Mo_{0.6}RhIrPt_2$, however an explanation is proposed below where Mo's smaller electronegativity distorts the DOS enough to shift the E_F to a region with fewer states: E_F is no longer in a linear region on the DOS and thus the T_c dissipates faster.

Figure 6:

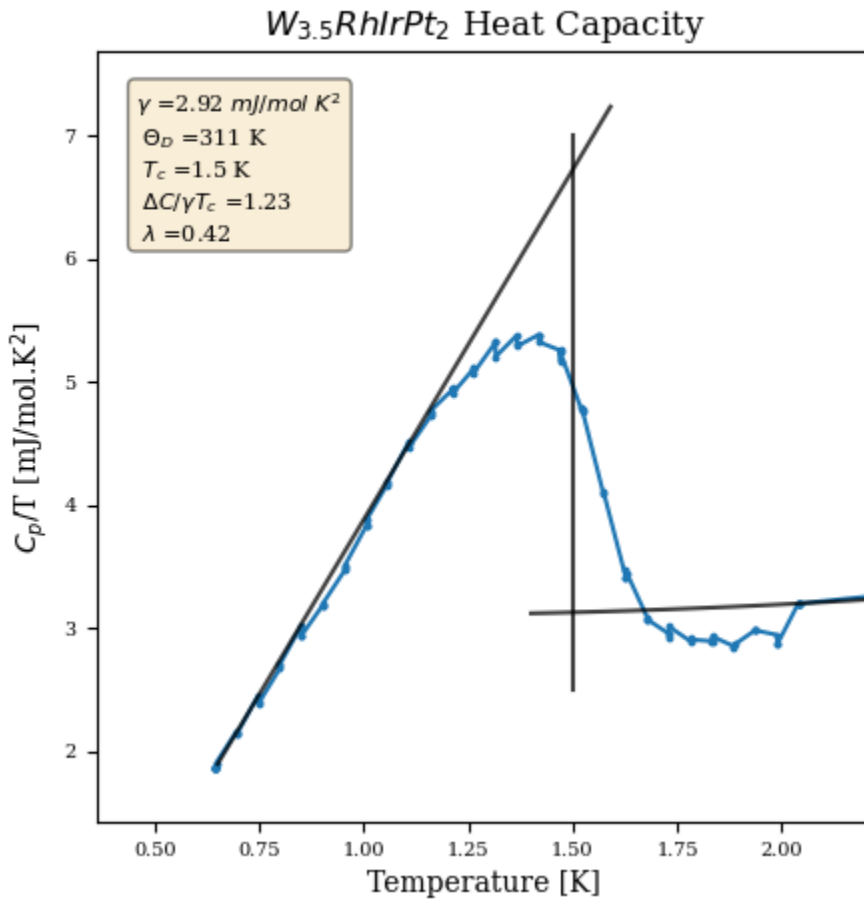


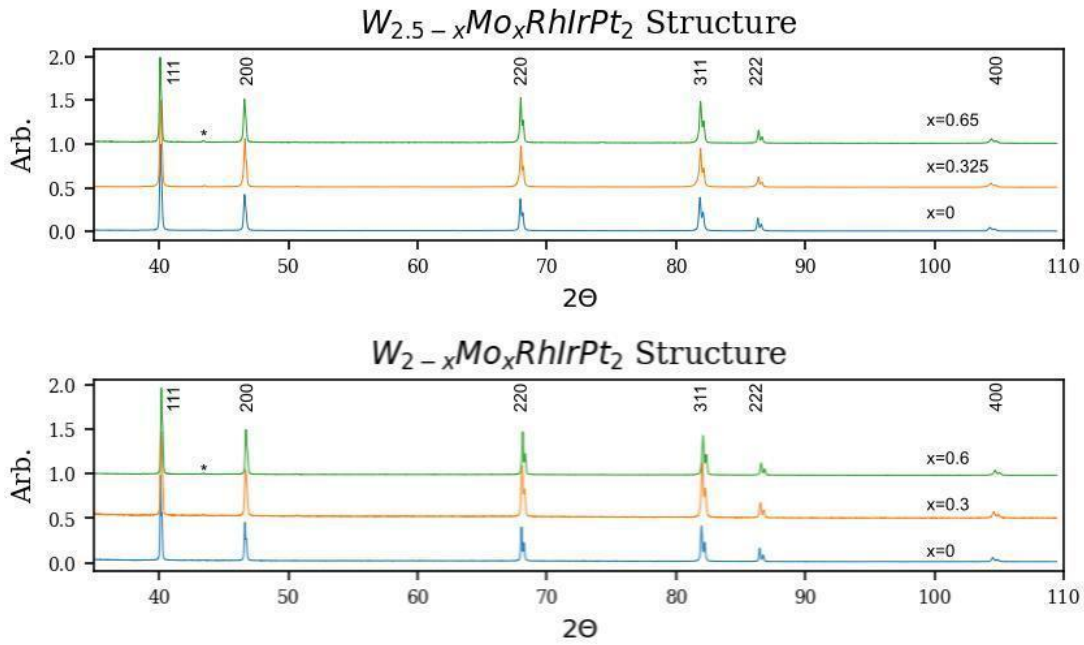
Figure 6: ³He data and analysis. Heat capacity for the W-rich alloy, W_{3.5}RhIrPt₂. There's a clear, broad superconducting transition following a Schottky anomaly. The high temperature region was fit to equation (5) and the low temperature to equation (7) resulting in $\Delta C_p/\gamma T_c \sim 1.23$, which is slightly low, but is paired with a low electron-phonon coupling of 0.42 calculated via equation (8).

Supplemental:

Enthalpy of Mixing values used in calculations (ref Cohesion in metals. Transition metal alloys by F.R. de Boer)

kJ/mol	Mo	W	Rh	Ir	Pt
Mo	0	0	-15	-21	-28
W	0	0	-9	-16	-20
Rh	-15	-9	0	1	-2
Ir	-21	-16	1	0	0
Pt	-28	-20	-2	0	0

Additional Diffractograms



*These high entropy versions look no different from the others provided in the main text. The * is an hcp impurity that has no effect on the interpretation of the data.*

W₄RhIrPt₂ Analysis:

Logical Formula	True Formula	a[Å]	δ	EN	Δχ	H _{mix} [kJ/mol]	S _{mix} [J/mol.K]	VEC	VEC spread	e/ab	T _c [K]	H _{c2} [T]	thickness [mm]
W4RhIrPt2	W50Rh12.5Ir12.5Pt25		0.96	2.31	0.02	-16.44	10.09	7.75	0.23	1.45	1.85	1.4	

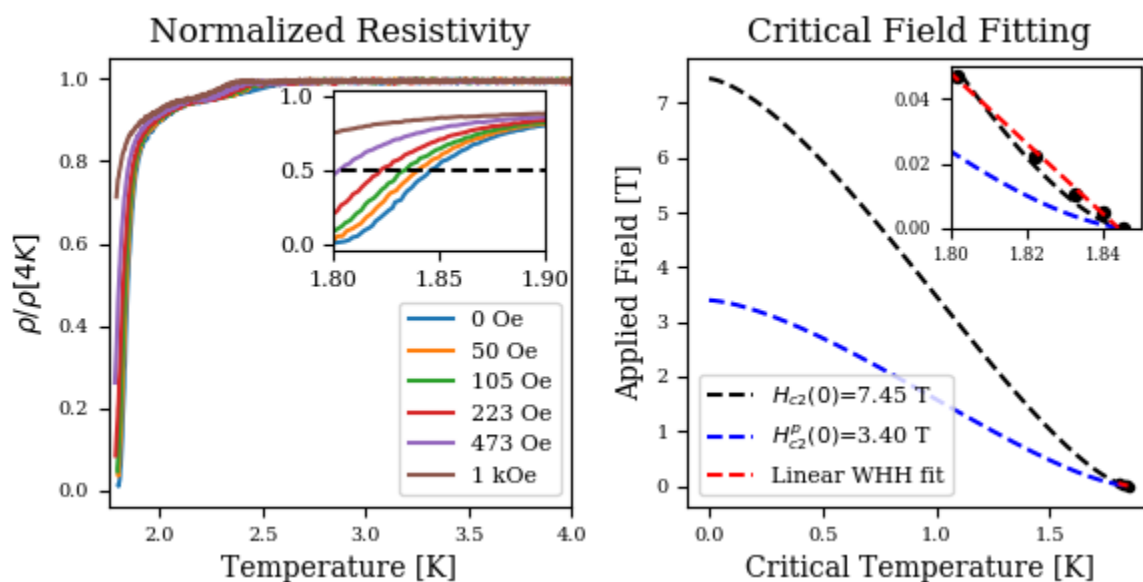


Figure S: Left) Normalized resistivity measurements for W₄RhIrPt₂ to 1.8 K at various fields. There is a slight impurity (undetectable by X Ray diffraction) that superconducts at 2.5 K in the samples that does not affect the overall interpretation. The inset focuses on the transitions near the 50% criterion; the intersections with the dotted line are translated to the right panel. **Right)** The transition temperatures are plotted associated as a function of applied field. The black dashed line was fit using equation 5. plotted by the blue dashed line. The red dashed line is a linear fit to determine the slope for the WHH approximation from equation 6 which reveals a sensible H_{c2}=1.40 T. **Not intrinsic!**

The resistivity systematically drops below 50% of the resistance of the normal state at multiple different applied magnetic fields. These transition temperatures are plotted versus applied field (figure S) and were be fitted to the expression,

$$H_{c2}(T) = H_{c2}(0) \left[1 - \left(\frac{T}{T_c} \right)^{\frac{3}{2}} \right]^{\frac{3}{2}}, \quad (5)$$

which has previously been used to determine the upper critical field in CsCl-type HEAs (ref). Using the few points accessible above the minimum experimentally attainable temperature, equation 5 yields an upper critical field, $H_{c2}(0)=7.45$ T, an extreme extrapolation. This is significantly larger than the expected Pauli limit of $H_{c2}=3.40$ T and thus would suggest that our FCC HEA superconductor may be an unusual one (ref). To elucidate this, the data can also be fit to the Werthamer-Helfand-Hohenburg (WHH) equation, which uses the slope of T_c vs T just below T_c to estimate the upper critical field,

$$\mu_0 H_{c2}(T) = -0.693 \mu_0 \left(\frac{dH_{c2}}{dT} \right)_{T=T_c} T_c \quad (6)$$

The calculated slope is $(dH_{c2}/dT)=-1.09$ T/K, which yields an upper critical field of 1.40 T, which is below the Pauli limit. The latter equation is a more reasonable estimate, as the WHH equation is used regularly for HEAs in the dirty limit and addresses the issue of spin-orbit coupling which is a legitimate possibility for heavy metals such as those in our FCC alloys (refs). Further an extreme extrapolation is not involved.

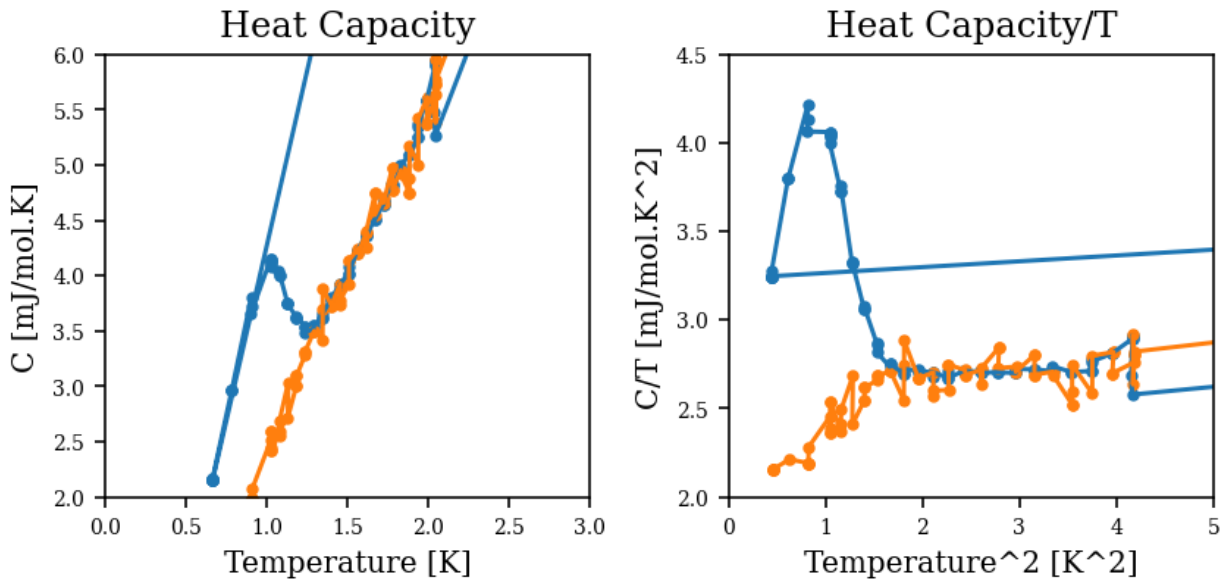


Figure 5 explanation

The tail for $W_{1.4}Mo_{0.6}RhIrPt_2$ is an artifact of the experiment. To collect the low temperature resistivity, an adiabatic refrigeration attachment was used. The process involves holding a 3 T magnetic field when cooling from 300 K. Once the machine is at 2 K, the field is linearly removed and the experiment begins recording. Since this sample has the lowest T_c , we suggest it also has a significantly low H_c and the magnetic field lines still penetrate the sample at low fields and temperatures. The tail is an artifact of decreasing magnetic field and increasing temperature.

List of values used in plots

compound	structure	Tc	delta	delta_H	VEC	Source Title
Ta ₃₄ Nb ₃₃ Hf ₈ Zr ₁₄ Ti ₁₁	bcc	7.3	4.57	2.5	4.67	Discovery of a superconducting high-entropy alloy
(TaNb) _{0.7} (HfZrTi) _{0.3}	bcc	8	4.35	2.38	4.7	Effect of electron count and chemical complexity in the Ta-Nb-Hf-Zr-Ti high-entropy alloy superconductor.
(TaNb) _{0.67} (HfZrTi) _{0.33}	bcc	7.8	4.48	2.51	4.67	Effect of electron count and chemical complexity in the Ta-Nb-Hf-Zr-Ti high-entropy alloy superconductor.
(TaNb) _{0.6} (HfZrTi) _{0.4}	bcc	7.6	4.72	2.72	4.6	Effect of electron count and chemical complexity in the Ta-Nb-Hf-Zr-Ti high-entropy alloy superconductor.
(TaNb) _{0.5} (HfZrTi) _{0.5}	bcc	6.5	4.93	2.83	4.5	Effect of electron count and chemical complexity in the Ta-Nb-Hf-Zr-Ti high-entropy alloy superconductor.
(TaNb) _{0.16} (HfZrTi) _{0.84}	bcc	4.5	4.65	1.52	4.16	Effect of electron count and chemical complexity in the Ta-Nb-Hf-Zr-Ti high-entropy alloy superconductor.
(TaNbV) _{0.67} (HfZrTi) _{0.33}	bcc	4.3	6.41	0.49	4.67	Effect of electron count and chemical complexity in the Ta-Nb-Hf-Zr-Ti high-entropy alloy superconductor.
(NbV) _{0.67} (HfZrTi) _{0.33}	bcc	7.2	7.05	-0.15	4.67	Effect of electron count and chemical complexity in the Ta-Nb-Hf-Zr-Ti high-entropy alloy superconductor.
(TaV) _{0.67} (HfZrTi) _{0.33}	bcc	4	7.05	-0.6	4.67	Effect of electron count and chemical complexity in the Ta-Nb-Hf-Zr-Ti high-entropy alloy superconductor.
(Sc _{0.33} Cr _{0.67} Nb) _{0.67} (HfZrTi) _{0.33}	bcc	5.6	9.15	0.2	4.67	Isoelectronic substitutions and aluminium alloying in the Ta-Nb-Hf-Zr-Ti high-entropy alloy superconductor
(TaSc _{0.33} Cr _{0.67}) _{0.67} (HfZrTi) _{0.33}	bcc	4.4	9.15	-0.54	4.67	Isoelectronic substitutions and aluminium alloying in the Ta-Nb-Hf-Zr-Ti high-entropy alloy superconductor
(TaNb) _{0.67} (Sc _{0.67} Cr _{0.33} ZrTi) _{0.33}	bcc	7.5	5.69	4.25	4.67	Isoelectronic substitutions and aluminium alloying in the Ta-Nb-Hf-Zr-Ti high-entropy alloy superconductor
(TaNb) _{0.67} (HfSc _{0.67} Cr _{0.33} Ti) _{0.33}	bcc	7.4	5.39	4.33	4.67	Isoelectronic substitutions and aluminium alloying in the Ta-Nb-Hf-Zr-Ti high-entropy alloy superconductor
(TaNb) _{0.67} (HfZrSc _{0.67} Cr _{0.33}) _{0.33}	bcc	7.6	6.16	4.71	4.67	Isoelectronic substitutions and aluminium alloying in the Ta-Nb-Hf-Zr-Ti high-entropy alloy superconductor
(Y _{0.33} Mo _{0.67} Nb) _{0.67} (HfZrTi) _{0.33}	bcc	4.7	8.96	6.82	4.67	Isoelectronic substitutions and aluminium alloying in the Ta-Nb-Hf-Zr-Ti high-entropy alloy superconductor
(TaY _{0.33} Mo _{0.67}) _{0.67} (HfZrTi) _{0.33}	bcc	3.5	8.95	6.23	4.67	Isoelectronic substitutions and aluminium alloying in the Ta-Nb-Hf-Zr-Ti high-entropy alloy superconductor

(TaNb) _{0.67} (Y _{0.67} Mo _{0.33} ZrTi) _{0.33}	bcc	7.6	7.27	7.44	4.67	Isoelectronic substitutions and aluminium alloying in the Ta-Nb-Hf-Zr-Ti high-entropy alloy superconductor
(TaNb) _{0.67} (HfY _{0.67} Mo _{0.33} Ti) _{0.33}	bcc	6.7	7.08	7.54	4.67	Isoelectronic substitutions and aluminium alloying in the Ta-Nb-Hf-Zr-Ti high-entropy alloy superconductor
(TaNb) _{0.67} (HfZrY _{0.67} Mo _{0.33}) _{0.33}	bcc	7.5	7.49	7.9	4.67	Isoelectronic substitutions and aluminium alloying in the Ta-Nb-Hf-Zr-Ti high-entropy alloy superconductor
(Sc _{0.33} Mo _{0.67} Nb) _{0.67} (HfZrTi) _{0.33}	bcc	4.4	6.62	2.87	4.67	Isoelectronic substitutions and aluminium alloying in the Ta-Nb-Hf-Zr-Ti high-entropy alloy superconductor
(TaSc _{0.33} Mo _{0.67}) _{0.67} (HfZrTi) _{0.33}	bcc	2.9	6.61	2.43	4.67	Isoelectronic substitutions and aluminium alloying in the Ta-Nb-Hf-Zr-Ti high-entropy alloy superconductor
(TaNb) _{0.67} (Sc _{0.67} Mo _{0.33} ZrTi) _{0.33}	bcc	7.5	5.11	4.64	4.67	Isoelectronic substitutions and aluminium alloying in the Ta-Nb-Hf-Zr-Ti high-entropy alloy superconductor
(TaNb) _{0.67} (HfSc _{0.67} Mo _{0.33} Ti) _{0.33}	bcc	6.6	4.79	4.71	4.67	Isoelectronic substitutions and aluminium alloying in the Ta-Nb-Hf-Zr-Ti high-entropy alloy superconductor
(TaNb) _{0.67} (HfZrSc _{0.67} Mo _{0.33}) _{0.33}	bcc	7.5	5.59	5.14	4.67	Isoelectronic substitutions and aluminium alloying in the Ta-Nb-Hf-Zr-Ti high-entropy alloy superconductor
Ta _{0.167} Nb _{0.333} Hf _{0.167} Zr _{0.167} Ti _{0.167}	bcc	7.9	4.93	3	4.5	Strongly correlated and strongly coupled s-wave superconductivity of the high entropy alloy Ta _{1/6} Nb _{2/6} Hf _{1/6} Zr _{1/6} Ti _{1/6} compound
Nb _{22.1} Ta _{26.3} Ti _{16.6} Zr _{15.5} Hf _{19.5}	bcc	7.1	4.92	2.81	4.48	Superconducting in equal molar NbTaTiZr-based high-entropy alloys
Nb _{21.5} Ta _{18.1} Ti _{15.9} Zr _{14.4} Hf _{16.6} V _{13.5}	bcc	5.1	6.22	1.25	4.53	Superconducting in equal molar NbTaTiZr-based high-entropy alloys
NbTaTiZrFe	bcc	6.9	8.06	-10.08	5.2	Superconducting in equal molar NbTaTiZr-based high-entropy alloys
NbReZrHfTi	bcc	5.3	5.87	-16.96	4.8	Superconductivity in equimolar Nb-Re-Hf-Zr-Ti high entropy alloy
Hf ₂₁ Nb ₂₅ Ti ₁₅ V ₁₅ Zr ₂₄	bcc	5.3	6.8	0.94	4.4	New high-entropy alloy superconductor Hf ₂₁ Nb ₂₅ Ti ₁₅ V ₁₅ Zr ₂₄
Mo _{0.2375} Re _{0.2375} Ru _{0.2375} Rh _{0.2375} Ti _{0.05}	hcp	3.6	2	-13.79	7.32	Superconductivity in high and medium entropy alloys based on MoReRu
Mo _{0.225} Re _{0.225} Ru _{0.225} Rh _{0.225} Ti _{0.1}	hcp	4.7	2.55	-18.25	7.15	Superconductivity in high and medium entropy alloys based on MoReRu
Mo _{0.1} Re _{0.1} Ru _{0.55} Rh _{0.1} Ti _{0.15}	hcp	2.1	3.16	-22.97	7.2	Superconductivity in high and medium entropy alloys based on MoReRu
Mo _{0.105} Re _{0.105} Ru _{0.527} Rh _{0.105} Ti _{0.158}	hcp	2.2	3.21	-23.72	7.16	Superconductivity in high and medium entropy alloys based on MoReRu
Mo _{0.118} Re _{0.118} Ru _{0.47} Rh _{0.118} Ti _{0.176}	hcp	2.5	3.31	-25.23	7.06	Superconductivity in high and medium entropy alloys based on MoReRu
Re _{0.56} Nb _{0.11} Ti _{0.11} Zr _{0.11} Hf _{0.11}	hcp	4.4	6	-28.1	5.79	Superconductivity in a new hexagonal high-entropy alloy
Nb ₁₀ Mo ₃₅ Ru ₃₅ Rh ₁₀ Pd ₁₀	hcp	5.6	1.94	-20.54	7.3	Superconductivity in hexagonal Nb-Mo-Ru-Rh-Pd high-entropy alloys.

Nb ₁₅ Mo _{32.5} Ru _{32.5} Rh ₁₀ Pd ₁₀	hcp	6.2	2.2	-23.93	7.2	Superconductivity in hexagonal Nb-Mo-Ru-Rh-Pd high-entropy alloys.
Nb ₂₀ Mo ₃₀ Ru ₃₀ Rh ₁₀ Pd ₁₀	hcp	6.1	2.4	-26.92	7.1	Superconductivity in hexagonal Nb-Mo-Ru-Rh-Pd high-entropy alloys.
Nb ₅ Mo ₃₅ Re ₁₅ Ru ₃₅ Rh ₁₀	hcp	7.54	1.58	-15.43	7.1	Structural evolution and superconductivity tuned by valence electron concentration in the Nb-Mo-Re-Ru-Rh high-entropy alloys
Nb ₅ Mo ₃₀ Re ₂₀ Ru ₃₅ Rh ₁₀	hcp	6.69	1.6	-14.61	7.15	Structural evolution and superconductivity tuned by valence electron concentration in the Nb-Mo-Re-Ru-Rh high-entropy alloys
Nb ₅ Mo ₂₅ Re ₂₅ Ru ₃₅ Rh ₁₀	hcp	6.51	1.62	-13.65	7.2	Structural evolution and superconductivity tuned by valence electron concentration in the Nb-Mo-Re-Ru-Rh high-entropy alloys
Nb ₅ Mo ₂₀ Re ₃₀ Ru ₃₅ Rh ₁₀	hcp	5.46	1.64	-12.55	7.25	Structural evolution and superconductivity tuned by valence electron concentration in the Nb-Mo-Re-Ru-Rh high-entropy alloys
(ZrNb) _{0.2} (MoReRu) _{0.8}	a-Mn	4.2	5.41	-24.55	6.5	High-entropy alloy superconductors on an a-Mn lattice.
(ZrNb) _{0.1} (MoReRu) _{0.9}	a-Mn	5.3	4.11	-18.26	6.75	High-entropy alloy superconductors on an a-Mn lattice.
(HfTaWIr) _{0.4} Re _{0.6}	a-Mn	4	4.48	-20.48	6.6	High-entropy alloy superconductors on an a-Mn lattice.
(HfTaWIr) _{0.3} Re _{0.7}	a-Mn	4.5	3.96	-16.09	6.7	High-entropy alloy superconductors on an a-Mn lattice.
(HfTaWIr) _{0.25} Re _{0.75}	a-Mn	5.6	3.65	-13.72	6.75	High-entropy alloy superconductors on an a-Mn lattice.
(HfTaWPt) _{0.4} Re _{0.6}	a-Mn	4.4	4.37	-22.32	6.7	High-entropy alloy superconductors on an a-Mn lattice.
(HfTaWPt) _{0.3} Re _{0.7}	a-Mn	5.7	3.89	-17.2	6.78	High-entropy alloy superconductors on an a-Mn lattice.
Nb ₂₅ Mo ₅ Re ₃₅ Ru ₂₅ Rh ₁₀	a-Mn	4.66	2.48	-25.85	6.9	Structural evolution and superconductivity tuned by valence electron concentration in the Nb-Mo-Re-Ru-Rh high-entropy alloys
Nb ₂₅ Mo ₁₀ Re ₃₅ Ru ₂₀ Rh ₁₀	a-Mn	5.1	2.41	-25.26	6.8	Structural evolution and superconductivity tuned by valence electron concentration in the Nb-Mo-Re-Ru-Rh high-entropy alloys
Nb ₂₅ Mo ₁₅ Re ₃₅ Ru ₁₅ Rh ₁₀	a-Mn	5.1	2.34	-24.39	6.7	Structural evolution and superconductivity tuned by valence electron concentration in the Nb-Mo-Re-Ru-Rh high-entropy alloys
Ta ₅ (Mo ₃₅ W ₅)Re ₃₅ Ru ₂₀	sigma	6.3	1.45	-11.97	6.7	Formation and superconductivity of single-phase high-entropy alloys with a tetragonal structure
Ta ₅ (Mo ₃₀ W ₁₀)Re ₃₅ Ru ₂₀	sigma	6.2	1.45	-11.62	6.7	Formation and superconductivity of single-phase high-entropy alloys with a tetragonal structure
Ta ₅ (Mo ₂₅ W ₁₅)Re ₃₅ Ru ₂₀	sigma	6.1	1.45	-11.2	6.7	Formation and superconductivity of single-phase high-entropy alloys with a tetragonal structure
Ta ₅ (Mo ₂₀ W ₂₀)Re ₃₅ Ru ₂₀	sigma	5.7	1.45	-10.92	6.7	Formation and superconductivity of single-phase high-entropy alloys with a tetragonal structure

Ta5(Mo15W25)Re35Ru20	sigma	5.5	1.45	-10.57	6.7	Formation and superconductivity of single-phase high-entropy alloys with a tetragonal structure
Ta5(Mo10W30)Re35Ru20	sigma	5.5	1.45	-10.22	6.7	Formation and superconductivity of single-phase high-entropy alloys with a tetragonal structure
Ta5(Mo5W35)Re35Ru20	sigma	4.8	1.44	-9.87	6.7	Formation and superconductivity of single-phase high-entropy alloys with a tetragonal structure
(Ta7Mo33)W5Re35Ru20	sigma	6.1	1.59	-12.99	6.68	Formation and superconductivity of single-phase high-entropy alloys with a tetragonal structure
(Ta9Mo31)W5Re35Ru20	sigma	5.7	1.71	-13.99	6.66	Formation and superconductivity of single-phase high-entropy alloys with a tetragonal structure
(Ta11Mo29)W5Re35Ru20	sigma	5.3	1.82	-14.97	6.64	Formation and superconductivity of single-phase high-entropy alloys with a tetragonal structure
(Ta13Mo27)W5Re35Ru20	sigma	5.3	1.92	-15.94	6.62	Formation and superconductivity of single-phase high-entropy alloys with a tetragonal structure
Ta10Mo30Cr5Re35Ru20	sigma	4.79	2.62	-14.56	6.65	Superconductivity and paramagnetism in Cr-containing tetragonal high entropy alloys
Ta10Mo25Cr10Re35Ru20	sigma	4.41	3.21	-14.31	6.65	Superconductivity and paramagnetism in Cr-containing tetragonal high entropy alloys
Ta10Mo22Cr13Re35Ru20	sigma	3.98	3.49	-14.16	6.65	Superconductivity and paramagnetism in Cr-containing tetragonal high entropy alloys
W46.7Rh13.3Ir13.3Pt26.7	fcc	1.56	0.99	-16.40	7.87	This text
W42.9Rh14.3Ir14.3Pt28.6	fcc	1.10	1.02	-16.17	8.00	This text
W37.9Mo5Rh14.3Ir14.3Pt28.6	fcc	1.25	1.03	-16.94	8.00	This text
W38.5Rh15.4Ir15.4Pt30.8	fcc	0.90	1.06	-15.68	8.15	This text
W33.5Mo5Rh15.4Ir15.4Pt30.8	fcc	0.85	1.07	-16.51	8.15	This text
W28.5Mo10Rh15.4Ir15.4Pt30.8	fcc	0.85	1.07	-17.34	8.15	This text
W33.3Rh16.7Ir16.7Pt33.3	fcc	0.45	1.11	-14.77	8.33	This text
W28.3Mo5Rh16.7Ir16.7Pt33.3	fcc	0.40	1.11	-15.67	8.33	This text
W23.3Mo10Rh16.7Ir16.7Pt33.3	fcc	0.30	1.11	-16.57	8.33	This text